CHINESE OPTICS LETTERS

Vol. 19, No. 2 | February 2021

Experimental and theoretical study of linearly polarized Lorentz–Gauss beams with heterogeneous distribution

Guanxue Wang (王冠学), Yu Miao (苗 玉), Yang Li (李 阳), Xinzhi Shan (单新治), and Xiumin Gao (高秀敏)*

School of Optical-Electrical and Computer Engineering, University of Shanghai for Science and Technology, Shanghai 200093, China

*Corresponding author: gxm@usst.edu.cn

Received June 16, 2020 | Accepted September 22, 2020 | Posted Online December 10, 2020

The unevenly distributed Lorentz–Gaussian beams are difficult to reproduce in practice, because they require modulation in both amplitude and phase terms. Here, a new linearly polarized Lorentz–Gauss beam modulated by a helical axicon (LGB-HA) is calculated, and the two various experimental generation methods of this beam, Fourier transform method (FTM) and complex-amplitude modulation (CAM) method, are depicted. Compared with the FTM, the CAM method can modulate the phase and amplitude simultaneously by only one reflection-type phase-only liquid crystal spatial light modulator. Both of the methods are coincident with the numerical results. Yet CAM is simpler, efficient, and has a higher degree of conformance through data comparison. In addition, considering some barriers exist in shaping and reappearing the complicated Lorentz–Gauss beam with heterogeneous distribution, the evolution regularities of the beams with different parameters (axial parameter, topological charge, and phase factor) were also implemented.

Keywords: Lorentz-Gauss beams; Fourier transform method; complex-amplitude modulation; spatial light modulator.
DOI: 10.3788/COL202119.022602

1. Introduction

With high brightness, purity of color, and strong directional transmission, the Gaussian beam has been widely used in many fields, such as laser processing[1–3], laser precision measurement[4–8], optical information processing[9–13], holography[14,15], and optical communication[16,17]. Semiconductor lasers in the field of photo-electronic technology status and development trends of other lasers have been irreplaceable, which is an important source of epoch-making significance. There is an important problem in the manufacturing process of semiconductor lasers. Due to the asymmetry of the incident beam of semiconductor lasers, a special optical shaping system needs to be adopted during the fabrication process, and it is necessary to understand its far-field beam characteristics while designing optical elements and conducting optical coupling[18]. In general, a simple Gaussian model is widely used in the study of the coupling efficiency of semiconductor lasers and optical fibers[19], but it is not suitable to represent the far-field distribution perpendicular to the junction direction due to the limitation of the small dispersion angle[20]. Dumke[21] found that under the same spatial distribution, dispersion angles of Lorentz–Gaussian distribution are bigger than that of Gaussian distribution, so the particularity of Lorentz–Gaussian distribution makes it more suitable to characterize the far-field distribution of semiconductor lasers.

As a result, with a strong expansibility, Lorentz–Gauss beams (LGBs) deserve deep and extensive studies[22]. Its properties have been fully exploited. In the non-paraxial case, the far-field propagation characteristics have been derived[22–24]. In the paraxial case[25], beam transmission factors of Lorentz beams are confirmed to be $\sqrt{2}$. Jiang *et al.* verified the Rayleigh scattering state of highly focused LGBs on dielectric microspheres[26]. So, LGBs modulated by a helical axicon (LGB-HA), like Lorentz–Gauss vortex beams, are then introduced and attract sufficient attention[27–29]. Chief among these, this kind of beam can exhibit heterogeneous distribution, such as distorted wavefront or asymmetric amplitude distribution modes as well as uneven spots around the singularity in the context of the beam parameter transformation[30,31]. These foundations have been applied in construction and transmission[32], far-field vector construction[33], partial coherence[34], and vortex characteristics[35]. Applying the vector diffraction theory, focusing properties of this kind beam have been demonstrated enough, but with few experimental validations.

In general, we can conduct wavefront phase modulation of Gaussian beams to reproduce some beams with good symmetry

and high uniformity, such as Airy beams, vortex beams, Hermite beams, and Bessel beams[36–38]. However, in the generation experiments of LGB-HA, the uneven distribution will be reproduced by at least two steps. The first step: convert the Gaussian amplitude to the asymmetric Lorentz–Gauss amplitude; the second step: overlay the distorted wavefront phase. To wit, a complex device is essential for simultaneously regulating the non-uniform distribution mode. But, we want to effectively control the complex optical field by a simple device.

In this paper, we not only explore the expressions and numerical simulations of LGB-HA but illustrate two generation methods, the Fourier transform method (FTM) and complex-amplitude modulation (CAM) method. Both of the approaches have the advantages of arbitrary dynamic and programmable modulations. In fact, the former is just the object light holographic reproduction, yet the latter controls beams by mixing the phase and amplitude terms together. CAM replaces the traditional method of modulating the amplitude and phase separately with two spatial light modulators (SLMs) and is a more efficient and flexible approach. Its coincidence degree with simulation results is higher than that of FTM. Therefore, this method can expand its application fields, exhibiting not only theoretical significance but practical value.

2. Generation Mechanism of LGB-HA in FTM and CAM

To facilitate the research, the polarization of LGBs studied in this paper is the linear polarization state. Electric-field amplitude distribution is determined by Lorentz and Gauss functions[39], expressed as

$$E(x_0,y_0)=E(x_0)E(y_0)=\exp\left(-\frac{x_0^2}{\omega_0^2}\right)\frac{\gamma_0^2}{\gamma_0^2+y_0^2}, \tag{1}$$

where ω_0 and γ_0 are a $1/e$ width of Gaussian distribution and a half-width of Lorentz distribution, respectively. To simplify the calculation, electric-field distribution of LGBs in the Cartesian coordinate system will be transformed to the cylindrical coordinate system, shown as[21]

$$E_0(\theta,f)=\exp\left(-\frac{\cos^2 f\cdot\sin^2\theta}{NA^2\cdot\omega_x^2}\right)\cdot\frac{1}{1+\frac{\sin^2 f\cdot\sin^2\theta}{NA^2\cdot\gamma_y^2}}, \tag{2}$$

where the tangential angle along the z axis is $\theta\in[0,\arcsin(NA)]$, and the azimuthal angle is $\phi\in[0,2\pi)$. NA is the numerical aperture. $\omega_x=\omega_0/\gamma_p$ is the relative Gaussian parameter, and $\gamma_y=\gamma_0/\gamma_p$ refers to the relative Lorentz parameter. γ_p is the outer radius of the optical aperture in the focusing system.

According to the diffraction theory, the electric field of LGBs with complex phase can be derived as[40–45]

$$\begin{aligned}\vec{E}(\rho,\psi,z)=\frac{1}{\lambda}\iint\{&[\sin^2\phi(1-\cos\theta)]\vec{x}\\&+\cos\phi\sin\phi(\cos\theta-1)\vec{y}+\cos\phi\sin\theta\vec{z}\}\\&\cdot\exp\left(-\frac{\cos^2\phi\cdot\sin^2\theta}{NA^2\cdot\omega_x^2}\right)\cdot\frac{1}{1+\frac{\sin^2\phi\cdot\sin^2\theta}{NA^2\cdot\gamma_y^2}}\\&\cdot\exp(iB\cdot NA^{-1}\cdot\sin\theta+im\phi)\\&\cdot\exp[i\pi\sin(n\phi)+i\pi\cos(n\phi)]\\&\cdot\exp[-ik\rho\sin\theta\cos(\phi-\psi)]\\&\cdot\exp(-ikz\cos\theta)\sin\theta\cos^{1/2}\theta\mathrm{d}\theta\mathrm{d}\phi,\end{aligned} \tag{3}$$

where the transmittance of helical axicon $\exp(iB\cdot NA^{-1}\cdot\sin\theta+im\phi)$ is equal to $\exp(ibr+im\phi)$. B is the dimensionless axicon parameter. Variables ρ,ψ, and z are the cylindrical coordinates of an observation point in the focal region. Vectors x, y, and z denote the unit vectors in the Cartesian coordinate system, respectively. n is the phase factor. Besides, $k=2\pi/\lambda$ is the wave number, and m is the topological charge of the spiral phase portion. It should be noted that $\exp(iB\cdot NA^{-1}\cdot\sin\theta+im\phi)\cdot\exp[i\pi\sin(n\phi)+i\pi\cos(n\phi)]$ is the heterogeneous phase modulation function.

2.1 Principle of FTM

To give a clear understanding of the generation methods, the mechanism of FTM is depicted. When $z=0$, the focus section of $E(\rho,\psi,z)$ provides the object wave function as $E(\rho,\psi)$. In the Cartesian coordinate system, $E(\rho,\psi)$ can be converted into $E_0(x_0,y_0)$. Fig. 1 shows the transforming process.

The SLM is represented by the square device. E_0 and E_i denote the hologram and the target light field, respectively. The lens with the distance d_0 to E_0 and d_1 to E_i is the Fourier lens. The target light field E_i can be Fourier transformed to the corresponding hologram E_0. The transformation process of LGBs can be uploaded on the phase-only SLM (P-SLM); the coded hologram can be inverted by a Fourier lens to achieve the original target light field.

In the circumstance of $d_0=d_i=f$, frequency-domain information can be obtained by applying Fourier transform to the object wave function. The transformation function is $E_i(x_i,y_i)=F\{E_0(x_0,y_0)\}$, which is mathematically written as

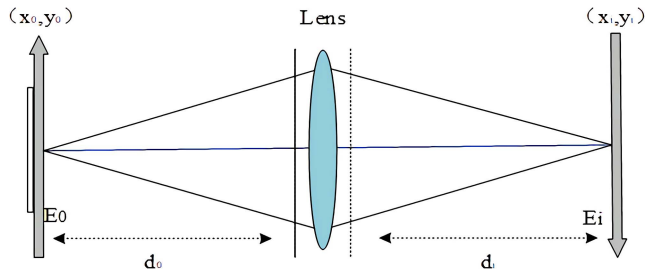

Fig. 1. Transition mechanism diagram of FTM.

$$E_i(x_i,y_i) = \frac{\exp(j2\,kf)}{j\lambda f}\int_{-\infty}^{\infty}\int E_0(x_0,y_0)\exp\left[-j\frac{2\pi}{\lambda f}(x_0x_i+y_0y_i)\right]\mathrm{d}x_0\mathrm{d}y_0. \tag{4}$$

$E_i(x_i,y_i)$ reveals frequency-domain information. The phase information modulation in the frequency domain can be expressed as

$$P = \mathrm{angle}[E_i(x_i,y_i)]/\max\{\mathrm{angle}[E_i(x_i,y_i)]\}\times 2\pi, \tag{5}$$

where the modulation range is $[0,2\pi)$. The angle $[E_i(x_i,y_i)]$ is the phase angle, and P is the normalized phase diagram.

Finally, frequency domain can be converted back to space domain via inverse Fourier transform, and the transfer function is derived as

$$E_0(x_0,y_0) = F^{-1}\{E_i(x_i,y_i)\}. \tag{6}$$

2.2 Principle of CAM

In traditional methods, at least two SLMs are required to modulate complex light fields. Starting from the perspective of phase, CAM can adjust both amplitude and phase functions only by a P-SLM[43]. Coded SLM can effectively adjust the properties of light beams, such as amplitude, polarization, and phase. Based on liquid crystals (LCs) properties, it can be implemented either upon the reflection or transmission mode. In fact, we need to calculate the transmittance function to get the phase diagram, in which each coordinate point (x, y) of the transmittance function corresponds to 0–255 colors of the phase diagram. When the incident light field interacts with LCs, the transmittance function can be presented with the reflection or transmission mode of LCs so as to modulate the light field.

Based on the above mechanism, P-SLM is used in this paper. Firstly, it is easy to understand the modulation principle of P-SLM, in which the phase programmed on the hologram is simply mod $[\Phi_2-\Phi_1, 2\pi]$ ($\Phi_2-\Phi_1$ is the phase difference between the initial light field and the target light field).

Secondly, it can be noted that in amplitude modulation the SLM cannot create light, so only a decrease in amplitude can be realized. When the phase depth of the hologram at some position changes $[2\pi, 2\pi\times C]$, the efficiency will accordingly change too (it is the fraction of power in the nth order, M is a constant). If $M=1$, then nearly 100% light will show up to the first order. If $M=0$, then 100% light will show up to the zero order.

To sum up, zero-order light spots can be successfully eliminated by the CAM method, and the target light field can be obtained by amplitude and phase modulation. Complex-amplitude distributions of LGB-HA can be defined as

$$U(x,y) = A_{\mathrm{LGB-HA}}\exp(i\phi_{\mathrm{LGB-HA}}), \tag{7}$$

with

$$A_{\mathrm{LGB-HA}} = \exp\left(-\frac{\cos^2\beta\cdot\sin^2\alpha}{NA^2\cdot\omega_x^2}\right)\cdot\frac{1}{1+\frac{\sin^2\beta\cdot\sin^2\alpha}{NA^2\cdot\gamma_y^2}},$$
$$\phi_{\mathrm{LGB-HA}} = \exp(iB\cdot NA^{-1}\cdot\sin\theta + im\phi)\cdot\exp[i\pi\sin(n\phi) + i\pi\cos(n\phi)], \tag{8}$$

where the amplitude item $A_{\mathrm{LGB-HA}}\in[0,1]$, and the phase item $\phi_{\mathrm{LGB-HA}}\in[-\pi,\pi]$. A combination of the amplitude and phase can be expressed by

$$h(x,y) = \exp[i\psi(A_{\mathrm{LGB-HA}},\phi_{\mathrm{LGB-HA}})], \tag{9}$$

where $\psi(A_{\mathrm{LGB-HA}},\phi_{\mathrm{LGB-HA}})$ represents the amplitude and phase covariant domain. In the ψ domain, the Fourier series expression is

$$h(x,y) = \sum_{-\infty}^{\infty} c_q^{A_{\mathrm{LGB-HA}}}\exp(iq\phi_{\mathrm{LGB-HA}}). \tag{10}$$

q is the positive integer. Thus, the first-order diffraction beam of LGB-HA is $c_1^{A_{\mathrm{LGB-HA}}} = A_{\mathrm{LGB-HA}}a$, where a is the location parameter. Besides, owing to $\psi(A_{\mathrm{LGB-HA}},\phi_{\mathrm{LGB-HA}})$ being odd, it can be converted to

$$\psi(A_{\mathrm{LGB-HA}},\phi_{\mathrm{LGB-HA}}) = f_{\mathrm{LGB-HA}}\sin(\phi_{\mathrm{LGB-HA}}). \tag{11}$$

Therefore, complex amplitude $h(x,y) = \exp[i\cdot f_{\mathrm{LGB-HA}}\cdot\sin(\phi_{\mathrm{LGB-HA}})]$ and its Fourier expansion is

$$\exp[if_{\mathrm{LGB-HA}}\sin(\phi_{\mathrm{LGB-HA}})] = \sum_{m=-\infty}^{\infty} J_m f_{\mathrm{LGB-HA}}\exp(im\phi_{\mathrm{LGB-HA}}). \tag{12}$$

J_m is equivalent to the m-order Bessel function. It can be verified as

$$A_{\mathrm{LGB-HA}} = J_1 f_{\mathrm{LGB-HA}}. \tag{13}$$

Eventually, LGB-HA can be encoded by P-SLMs as

$$\Phi_{\mathrm{SLM}} = f_{\mathrm{LGB-HA}}\sin(\Phi_{\mathrm{LGB-HA}} + G_xX + G_yY), \tag{14}$$

where G_x and G_y are grating constants along the x axis and y axis, respectively. CAM can produce the intricate beam through the modulation of the weight factor between phase and amplitude, indicating that two separate SLMs can be replaced by a P-SLM. With CAM, we can get arbitrary complex-amplitude beams, such as Ince beams, Bessel beams, and LGBs.

3. Experimental Setup and Result Analysis

Figure 2 depicts the schematic apparatus for generating LGB-HA.

In the experimental device in this paper, the laser used is linearly polarized and has a wavelength of 632.8 nm. The

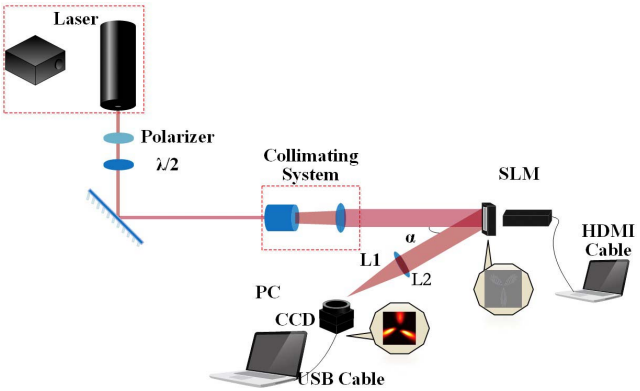

Fig. 2. Experiment setup. $\lambda/2$, half-wave plate; M, mirror; L1, lens with focal length of 100 mm; L2, lens with focal length of 300 mm; SLM, spatial light modulator; CCD, charge coupled device. The inset depicts the hologram of LGB-HA.

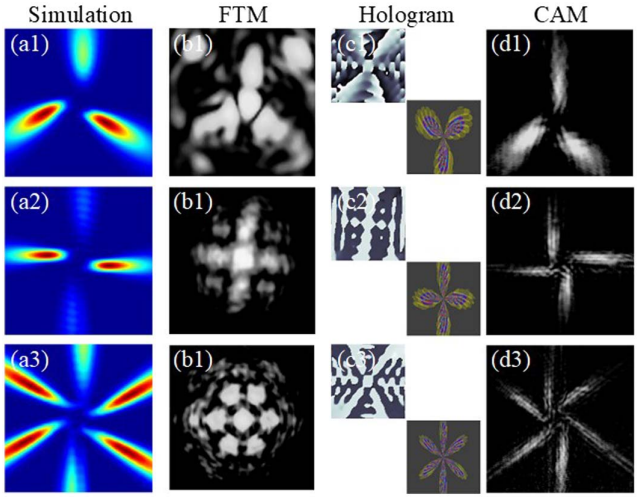

Fig. 3. Two methods for the generation of LGB-HA corresponding to numerical simulation under $NA = 0.09$, $B = 4$, $m = 3$, $\omega_x = 0.3$, $\gamma_p = 0.3$ with various phase factor n. (a1)–(a3) Numerical simulation results for $n = 3$, 4, and 6, respectively; (b1)–(b3) experimental results of FTM with phase parameter $n = 3$, 4, and 6; (c1)–(c3) phase patterns consist of the upper left corner mapping to FTM and the lower right corner mapping to CAM. (d1)–(d3) Experimental results of CAM with phase parameter n = 3, 4, and 6.

experiment consists of the half-wave plate (HWP, fast axis along angle $\theta \in [0,2\pi]$ and a polarizer, making the polarization direction of the beam locate in the effective response of the P-SLM (Holoeye SLM with 1920×1080 pixels). Horizontally polarized beams then are reflected into the collimating system, where the magnification of the beam expander is 10×, the numerical aperture is 0.25, and the collimating lens focal length is 100 mm. The aperture diaphragm can be placed to adjust the diameter of the expanded beam, located within the effective area of the P-SLM. The beams reflected from the P-SLM are transformed by a Fourier lens (focal length of 300 mm), and then the desired beams are discerned by a CCD (resolution 1292×964 pixels, pixel size 3.75×3.75 μm). It is of paramount importance that the angle between the reflection beam and the incident beam of the P-SLM is as small as possible.

Depending on the above descriptions, we can generate LGBs by two approaches. Intensity pattern of LGBs under different n is illustrated in Fig. 3. Simulation results demonstrate that the number of energy flow focus (EFF) carried by LGBs is proportional to the n. Figures 3(b1)–(b3) and 3(d1)–(d3) indicate the intensity distribution with $n = 3$, 4, and 6 using two different ways. Both of the columns can precisely exhibit the evolution principle of the focal pattern, which is in good agreement with simulation results. Nevertheless, interfering with diffraction phenomena of FTM is much more obvious than of CAM. So far, both approaches have met our expectations, which mean that LGBs with complex phase distribution can be achieved successfully. It is noteworthy that the left and right column phase cross sections that emerged in Figs. 3(c1)–(c3) indicate the huge differences in the two generation ways. Obviously, the degree of reduction of CAM is superior to FTM.

An obvious light spot emerged in FTM experimental results, shown in the second column in Fig. 3, which is caused by zero-order diffraction light. In the Fourier transform process, in order to ensure the accuracy of the inverse transformation, it is not appropriate to introduce additional modulation, such as gratings, to obtain holograms. Maybe zero-order diffraction light in FTM can be eliminated or transferred by complex optical systems, but this loses the significance of simplicity, high precision, and repeatability. What is more, the CAM method illustrated in this paper can realize the ideal non-uniform distribution without the interference of zero-order diffraction light.

Indicated from the evolution law of the focusing pattern above, the energy flow density of LGBs changes with the number of energy flow focal points. Subsequently, in contrast to Fig. 3, with lower phase parameters, arguments $n = 6$, 7, 8, and 20 are also sorted: one is for the sake of universal verification of the response law between intensity patterns and phase distribution, and the other is for showing whether the energy flow density is saturated or not, phase parameter n is large enough.

Figure 4 depicts four focus patterns corresponding to the phase parameters 6, 7, 8, and 20, respectively. Experimental results fully indicate that CAM can restore LGBs with high accuracy. In addition, EFF is proportional to the phase factor n with a positive correlation scoring +1, which is one step further for verifying the positive dependency between energy flow density of LGBs and n. This discipline is strongly consistent with the impact of different phase parameter n on phase distribution patterns discussed previously, which adequately verifies the validity of our theoretical research. As n increases, uneven distribution of energy flow density occurs; in particular, for $n = 20$, energy flow turbulence or any heterogeneous energy distribution hints that energy flow density of LGBs is saturated. Intriguingly, no matter how the phase factor n changes, there is an uneven intensity distribution in the focal plane, that is, the energy in the horizontal direction is higher than the energy in the vertical direction. In addition, when n is large enough ($n = 20$), a vortex-like structure appears again in center of the focus, and the

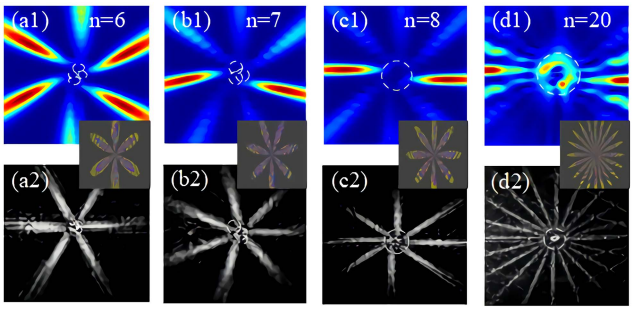

Fig. 4. Intensity distributions of LGB-HA corresponding to numerical simulation under $NA = 0.09$, $B = 4$, $m = 3$, $\omega_x = 0.3$, $\gamma_p = 0.3$ with different phase factor n. The upper layer is simulation results, the bottom layer is experiment results, and the middle layer is the complex amplitude hologram. Internal details emerge corresponding to the regions marked by the overlaid white circles.

whole energy remains non-uniform. It is notable that a part of energy flow intensity breaks up to a central semi-ring. Actually, the experiment has revealed the tendency of central speckle formation while n is small, shown in the bottom layer of Fig. 4, the regions marked by the overlaid white circles.

For intuitively comparing the consistency between the two methods and the simulation results, the normalized axis-directed energy distribution profiles in the focal plane of the simulation results, FTM as well as CAM, are given. With the fixed x-axis coordinate value, the normalized energy distribution plane along the y axis can be successfully intercepted, as shown in Fig. 5. We set $m = 3$, $B = 4$, $n = 6$, and the fixed $x = 100$.

Obviously, two intensity peaks appear in the focusing field along the x-axis direction, as shown in Fig. 5(a). FTM cannot eliminate the zero-order diffraction spot and has a weak ability of beam recovery, presenting three primary peaks and two side peaks in the energy profile, which is beyond the simulated two peaks [Fig. 5(b)]. On the contrary, in Figs. 5(a) and 5(c), CAM can completely preserve the basic structure and morphology of the spot, which makes our work more practical and significant.

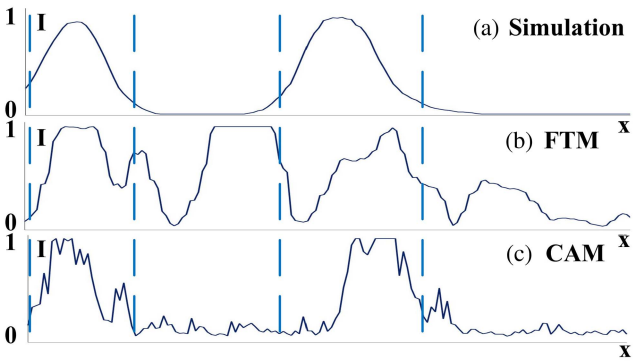

Fig. 5. Normalized axis-directed energy distribution profiles in the focal plane of the simulation results, FTM and CAM under $m = 3$, $B = 4$, $n = 6$. (a) Theoretical simulation results. (b) Experimental result of FTM. (c) Experimental result of CAM.

Both Figs. 5(b) and 5(c) are the original data without any algorithm modifications. The waveform jitter in Fig. 5(b) is caused by stray light in the optical system. Thus, a pure beam can be obtained through the corresponding filtering method, which is not repeated in this paper.

4. Conclusions

Two experimental approaches are utilized to generate LGBs with heterogeneous distribution and spiral phase. The experiments are consistent with the simulation results. A comparison of FTM and CAM is also investigated, confirming that CAM has high coincidence and detailed information, matching better with the numerical calculation. Furthermore, based on the numerical simulation, the axial parameter B, topological charge m, and phase factor n affect the focus shift, rotation of the intensity pattern, and energy flow density, respectively. We can control the focusing properties of LGBs and find out the optimal B, n, and m for practical applications in beam shaping, optical trapping and manipulation, and laser processing.

Acknowledgement

This work was supported partly by the National Key Research and Development Program (No. 2018YFC1313803).

References

1. S. Hasegawa, K. Shiono, and Y. Hayasaki, "Femtosecond laser processing with a holographic line-shaped beam," Opt. Express **23**, 23185 (2015).
2. G. C. Rodrigues and J. R. Duflou, "Into polarization control in laser cutting with direct diode lasers," J. Laser Appl. **28**, 022207 (2016).
3. A. Salama, L. Li, P. Mativenga, and A. Sabli, "High-power picosecond laser drilling/machining of carbon fibre-reinforced polymer (CFRP) composites," Appl. Phys. A **122**, 73 (2016).
4. Y. Liu, Y. Guo, J. Lin, G. Huang, C. Duan, and F. Li, "Measurement of the electric dipole moment of NO ($X^2\Pi\, v = 0, 1$) by mid-infrared laser magnetic resonance spectroscopy," Mol. Phys. **99**, 1457 (2001).
5. M. Mori, S. Kawamura, T. Ikeda, and W.-G. Jin, "Profile measurement of laser microbeam produced by glass capillaries," in *2019 24th Opto-Electronics and Communications Conference (OECC) and 2019 International Conference on Photonics in Switching and Computing (PSC)* (2019), p. 1.
6. W. Schweinberger, L. Vamos, J. Xu, S. A. Hussain, C. Baune, S. Rode, and I. Pupeza, "Interferometric delay tracking for low-noise Mach-Zehnder-type scanning measurements," Opt. Express **27**, 4789 (2019).
7. L.-M. Zhou, K.-W. Xiao, Z.-Q. Yin, J. Chen, and N. Zhao, "Sensitivity of displacement detection for a particle levitated in the doughnut beam," Opt. Lett. **43**, 4582 (2018).
8. Y. Hu, X. Liu, Y. Li, and M. Ding, "An electro-optic modulator detection method in all optical atomic magnetometer," in *Asia-Pacific Optical Sensors Conference* (2016), paper Tu3A.6.
9. J.-W. Zhou, P.-F. Wang, F.-Z. Shi, P. Huang, X. Kong, and X.-K. Xu, "Quantum information processing and metrology with color centers in diamonds," Front. Phys. **9**, 587 (2014).
10. L. Zhang, S. Bao, H. Zhang, G. Raithel, J. Zhao, L. Xiao,, and S. Jia, "Interplay between optical pumping and Rydberg EIT in magnetic fields," Opt. Express **26**, 29931 (2018).
11. H. Li, "Research on target information optics communications transmission characteristic and performance in multi-screens testing system," Opt. Commun. **364**, 139 (2016).

12. F. Flamini, N. Spagnolo, and F. Sciarrino, "Photonic quantum information processing: a review," Rep. Prog. Phys. **82**, 016001 (2018).
13. A. E. Willner, S. Khaleghi, M. R. Chitgarha, and O. F. Yilmaz, "All-optical signal processing," J. Lightwave Technol. **32**, 660 (2013).
14. H. Ou, Y. Wu, E. Lam, and B.-Z. Wang, "Enhanced edge extraction using spiral phase plate in optical scanning holography based on Gaussian beam apodization," in *Digital Holography and Three-Dimensional Imaging* (2017), paper W2A.26.
15. U. Ruiz, P. Pagliusi, C. Provenzano, and G. Cipparrone, "Vector beams generated by tunable liquid crystal polarization holograms," J. Appl. Phys. **121**, 153104 (2017).
16. J. Wang, "Advances in communications using optical vortices," Photon. Res. **4**, B14 (2016).
17. X. Yi, Z. Li, and Z. Liu, "Underwater optical communication performance for laser beam propagation through weak oceanic turbulence," Appl. Opt. **54**, 1273 (2015).
18. H. C. Casey, Jr. and M. B. Panish, *Heterostructure Lasers* (Academic, 1978).
19. H. Karstensen, "Laser diodes to single-mode fiber couping with ball lenses," J. Opt. Commun. **9**, 42 (1988).
20. D. D. Cook and F. R. Nash, "Gain-induced guiding and astigmatic output beam of GaAs lasers," J. Appl. Phys. **46**, 1660 (1975).
21. P. Dumke, "The angular beam divergence in double-henterojunction lasers with very thin active regions," J. Quantum Electron. **11**, 400 (1975).
22. O. E. Gawhary and S. Severini, "Lorentz beams and symmetry properties in paraxial optics," J. Opt. A: Pure Appl. Opt. **8**, 409 (2006).
23. D. Liu, H. Yin, and Y. Wang, "Nonparaxial propagation of a partially coherent Lorentz-Gauss beam," Optik **155**, 190 (2018).
24. X. Wang, Z. Liu, and D. Zhao, "Nonparaxial propagation of Lorentz–Gauss beams in uniaxial crystal orthogonal to the optical axis," J. Opt. Soc. Am. A **31**, 872 (2014).
25. G.-Q. Zhou, "Study on the propagation properties of Lorentz beam," Chin. J. Lasers **36**, 2326 (2008).
26. Y. Jiang, K. Huang, and X. Lu, "Radiation force of highly focused Lorentz-Gauss beams on a Rayleigh particle," Opt. Express **19**, 9708 (2011).
27. G. Zhou and G. Ru, "Angular momentum density of a linearly polarized Lorentz–Gauss vortex beam," Opt. Commun. **313**, 157 (2014).
28. D. Liu, H. Yin, G. Wang, and Y. Wang, "Propagation of partially coherent Lorentz–Gauss vortex beam through oceanic turbulence," Appl. Opt. **56**, 8785 (2017).
29. Y. Miao, G. Wang, X. Zeng, G. Sui, R. Zhang, and Q. Zhan, "Focusing properties of radially polarized helico-conical Lorentz-Gauss beam," Optik **136**, 289 (2017).
30. C. Kamacıoğlu and Y. Baykal, "Generalized expression for optical source fields," Opt. Laser Technol. **44**, 1706 (2012).
31. X. Zeng, Y. Miao, G. Wang, Q. Zhan, R. Hong, and R. Zhang, "Tunable optical gradient force of radially polarized Lorentz-Gauss vortex beam by sine-azimuthal variation wavefront," Optik **130**, 481 (2017).
32. G. Zhou, "Beam propagation factors of a Lorentz–Gauss beam," Appl. Phys. B **96**, 149 (2009).
33. G. Zhou, "Far-field properties of super-Lorentzian–Gauss mode beams," J. Opt. **12**, 035704 (2010).
34. D. Liu, G. Wang, and Y. Wang, "Average intensity and coherence properties of a partially coherent Lorentz-Gauss beam propagating through oceanic turbulence," Opt. Laser Technol. **98**, 309 (2018).
35. A. Torre, "Wigner distribution function of a Lorentz–Gauss vortex beam: alternative approach," Appl. Phys. B **122**, 55 (2016).
36. C. Wang, Y. Ren, T. Liu, L. L. Chen, and S. Qiu, "New kind of Hermite-Gaussian-like optical vortex generated by cross phase," Chin. Opt. Lett. **18**, 100501 (2020).
37. X. Yang, S. B. Wei, S. S. Kou, F. Yuan, and E. Cheng, "Misalignment measurement of optical vortex beam in free space," Chin. Opt. Lett. **17**, 090604 (2019).
38. G. X. Wang, Y. Li, X.Z. Shan, Y. Miao, and X. M. Gao, "Hermite-Gaussian beams with sinusoidal vortex phase modulation," Chin. Opt. Lett. **18**, 042601 (2020).
39. F. Rui, D. Zhang, M. Ting, X. Gao, and S. Zhuang, "Focusing of linearly polarized Lorentz–Gauss beam with one optical vortex," Optik-Int. J. Light Electron Opt. **124**, 2969 (2013).
40. B. Richards and E. Wolf, "Electromagnetic diffraction in optical systems. II. Structure of the image field in an aplanatic system," Proc. R. Soc. Lond. A **253**, 358 (1959).
41. W. Zhu, H. Guan, H. Lu, J. Tang, Z. Li, J. Yu, and Z. Chen, "Orbital angular momentum sidebands of vortex beams transmitted through a thin metamaterial slab," Opt. Express **26**, 17378 (2018).
42. V. Parigi, V. D'Ambrosio, C. Arnold, L. Marrucci, F. Sciarrino, and J. Laurat, "Storage and retrieval of vector beams of light in a multiple-degree-of-freedom quantum memory," Nat. Commun. **6**, 7706 (2015).
43. C. Hnatovsky, V. G. Shvedov, and W. Krolikowski, "The role of light-induced nanostructures in femtosecond laser micromachining with vector and scalar pulses," Opt. Express **21**, 12651 (2013).
44. S. N. Khonina, V. V. Kotlyar, V. A. Soifer, M. V. Shinkaryev, and G. V. Uspleniev, "Trochoson," Opt. Commun. **91**, 158 (1992).
45. A. Forbes, A. Dudley, and M. McLaren, "Creation and detection of optical modes with spatial light modulators," Adv. Opt. Photon. **8**, 200 (2016).